Available online at www.sciencedirect.com

ScienceDirect

Solar Energy 122 (2015) 727–736

SOLAR ENERGY

www.elsevier.com/locate/solener

Pt–Co and Pt–Ni hollow nanospheres supported with PEDOT:PSS used as high performance counter electrodes in dye-sensitized solar cells

Min Zheng [a], Jinghao Huo [a], Binguo Chen [a], Yongguang Tu [a], Jihuai Wu [a,*], Linhua Hu [b], Songyuan Dai [b]

[a] *Institute of Materials Physical Chemistry, Huaqiao University, Quanzhou 362021, China*
[b] *Hefei Institutes of Physical Science, CAS, 350 Shushanhu Road, Hefei 230031, China*

Received 4 July 2015; received in revised form 17 September 2015; accepted 5 October 2015
Available online 10 November 2015

Communicated by: Associate Editor Frank Nuesch

Abstract

Binary alloy platinum–cobalt (Pt–Co) and platinum–nickel (Pt–Ni) hollow nanospheres are prepared by using a simple solution reaction method. Poly(3,4-ethylenedioxy thiophene):polystyrene sulfonate (PEDOT:PSS) as supported layer further enhance the binary platinum alloy electrochemical properties. The prepared binary platinum alloys are observed with hollow nanosphere structure. The cyclic voltammogram and electrochemical impedance spectroscopy measurement indicate that Pt–Co and Pt–Ni hollow nanospheres on PEDOT:PSS (PC-PP and PN-PP) electrodes have high conductivity and catalytic performance. Under simulated white solar light irradiation with intensity of 100 mW cm^{-2} (AM 1.5), the dye-sensitized solar cells (DSSCs) based on PCPP and PNPP counter electrodes achieve power conversion efficiencies of 9.02% and 8.23%, respectively, which are higher than the efficiency for the DSSC based on Pt counter electrode (7.96%).

Keywords: Dye-sensitized solar cell; Platinum–cobalt alloy; Platinum–nickel alloy; Counter electrode

1. Introduction

Energy problem is the most serious challenge for human society, and the development of novel solar cell is an optimal method to solve the problem. Dye-sensitized solar cells (DSSCs) are promising photovoltaic devices due to their low cost, easy preparation, good performance and environmental benignity (Gratzel, 2001; Wu et al., 2015). Generally, a standard DSSC has three main components: a dye sensitized TiO_2 photoanode, an iodide/triiodide (I^-/I_3^-) redox electrolyte, and a counter electrode (CE). As a crucial component, the CE plays an important role to catalysis the reduction of triiodide ions in the electrolyte and to transmit charge carriers (Ahmad et al., 2014). Conductive fluorine doped tin oxide (FTO) glass deposited with platinum is a preferred CE owing to its superior conductivity, stability and electrocatalytic activity for the reduction of triiodide. However, large-scale application of DSSCs based on Pt CE is seriously hindered by its high cost and easy reaction with iodide/triiodide in electrolyte. Therefore, many substitute materials, such as carbon materials (Li et al., 2009; Anwar et al., 2013; Cruz et al., 2012), conductive polymer materials (Li et al., 2008; Wu et al., 2008a,b), transition metal carbides (Wu et al., 2011), transition metal sulfides (Chuang et al., 2014; Xiao et al., 2013; Lu et al., 2014) and transitional metal diseleniums (Gong et al.,

* Corresponding author. Tel.: +86 595 22693899; fax: +86 595 22692229.
E-mail address: jhwu@hqu.edu.cn (J. Wu).

http://dx.doi.org/10.1016/j.solener.2015.10.001
0038-092X/

2012, 2013), have been widely investigated to replace Pt, however, the effect is not satisfactory. Meanwhile, Pt-based CEs were also studied to enhance the performance or to reduce the amount of Pt. Chung et al. (Chih et al., 2012; Sui et al., 2012) reported the influences of textures in Pt CE and produced nanoporous Pt CE by glancing angle deposition. Wu et al. (Pin et al., 2008; Zi et al., 2012) prepared Pt/Carbon black CE and Pt/PANI CE to reduce the Pt content and the high-performance of DSSC remained.

Recently, Pt-based alloy materials attract much attention because of their good catalytic activities and high electrical conductivities. Tang and co-workers (He et al., 2014) reported the preparation of CoPt alloy CEs by electrochemical method. A promising power conversion efficiency of 10.23% was obtained by using an electro-chemically co-deposited $CoPt_{0.02}$ alloy CE. Fang et al. (Wan et al., 2014) demonstrated the catalytic activity of Pt–Ni for the reduction of I_3^- to I^- by solvent-based synthesis, and generated a promising efficiency of 8.78% in their DSSC device. In their opinion, alloying with inexpensive Ni might not only reduce the using of Pt metals but also facilitate the electron transfer between the CEs and I^-/I_3^- redox couples. At present, the study on bimetallic or multi-metal CEs is preliminary and further researches are on the way.

The metal hollow nanospheres have high specific surface area with low density and low cost, and have been used as the electrocatalyst in other areas (Chen et al., 2007; Jiao et al., 2014; Liu et al., 2009). The metal hollow nanospheres exhibit a good electrocatalytic performance and can be used as counter electrodes in DSSCs. Herein, binary alloy platinum–cobalt hollow nanospheres (PC-HN) and platinum–nickel hollow nanospheres (PN-HN) with very thin shell, about 2 nm, are synthesized by a facile solvent-based method at the room temperature. In order to enhance the electrochemical properties, PEDOT:PSS with good conductivity and catalytic properties are utilized as support layer. The DSSCs based on Pt–Co and Pt–Ni hollow nanospheres supported with PEDOT:PSS CE achieve power conversion efficiencies of 9.02% and 8.23%, respectively. Under the same condition, the efficiency for the DSSC based on Pt CE (7.96%) is lower than the DSSCs based on PCPP and PNPP CEs.

2. Experimental

2.1. Preparation of Pt–Co and Pt–Ni hollow nanospheres

PC-HN was prepared by using a simple method: citric acid ($C_6H_8O_7{\cdot}H_2O$, 8 mg, Aladdin, China, 99.5%) was dissolved in 100 ml deionized water, then cobalt chloride ($CoCl_2{\cdot}6H_2O$, 0.2 ml, 2 M, Aladdin, China, AR) aqueous solution was added into the $C_6H_8O_7$ aqueous solution, stirring vigorously for 5 min. Then, nitrogen was passed through the mixed solution for 30 min to remove most of oxygen. Freshly prepared sodium borohydride ($NaBH_4$, Sinopharm Chemical Reagent Co. Ltd., China, 96%) aqueous solution (1 ml, 13 mg ml^{-1}) was added quickly to the $CoCl_2$ solution under vigorous stirring and nitrogen atmosphere protecting. When the system turned black, chloroplatinic acid (H_2PtCl_6, 20 ml, 1.6 mM, Sinopharm Chemical Reagent Co. Ltd., China, AR) aqueous solution was added dropwise. After stirring 120 min, the products were collected by centrifugation and washed three times with ethanol, thus PC-HN was obtained. The PN-HN was prepared by using the same method.

2.2. Preparation of counter electrodes

The preparation process of counter electrode (CE) is shown in Fig. 1. PEDOT:PSS (Aldrich, 1.3% dispersion in H_2O) was filtered by using a hydrophilic syringe filter (0.45 μm) to remove large-size particles. The filtrate was spin-cast onto 1.5 × 1.5 cm^2 FTO glasses (Fluorine doped tin oxide over-layer, sheet resistance 14 $\Omega\,\square^{-1}$, Nippon Glass Co. Japan) at 4000 rpm and then dried at 120 °C for 15 min. The PEDOT:PSS film (about 100 nm) was treated by immersing the film into a concentrated sulfuric acid (H_2SO_4) solution for 10 min at room temperature to remove most of PSS (Kim et al., 2014). The film was sufficiently washed with a deionized water and ethanol bath, lastly, dried at 120 °C for 10 min, then a substrate with PEDOT:PSS thin layer was obtained. The Pt–Co hollow spheres obtained above was dispersed in 4 ml ethanol under ultrasonic for 10 min and spin-coated onto the PEDOT:PSS film at 2000 rpm for 2 times, dried at 60 °C. Lastly, PC-HN on PEDOT:PSS film (PC-PP) counter electrode was obtained. Similarly, a PN-HN on PEDOT:PSS film (PN-PP) counter electrode also was obtained. For comparing, PC-HN on FTO glass without PEDOT:PSS film (PC), PN-HN on FTO glass without PEDOT:PSS film (PN), and H_2SO_4-treated PEDOT:PSS (HPP) substrate also was used as counter electrodes. For comparison, Pt CE was prepared by heating Pt precursor solution spreading out on a FTO glass at 400 °C for 30 min. The precursor solution contained 5-mg $H_2PtCl_6{\cdot}6H_2O$ in 1-ml 2-propanol (Gao et al., 2014).

2.3. Preparation of TiO_2 photoanode and fabrication of DSSCs

Ultrafine TiO_2 (size: 3–4 nm) toluene solution and a nanometer TiO_2 (size: 10–20 nm) colloid solution were synthesized according to our prior work (Que et al., 2014; Wu et al., 2008a,b, 2007). TiO_2 blocking layer was solidified onto the FTO glass by spin coating the ultrafine TiO_2 toluene solution at 3500 rpm for 2 times and sintering at 450 °C for 30 min in the air. TiO_2 mesoporous layer with thickness of 6–8 μm was deposited on the TiO_2 blocking layer by coating the TiO_2 colloid using a doctor blade technique, then sintered at 450 °C for 30 min in the air. After being cooled naturally to room temperature, the film was immersed into the 0.05 M $TiCl_4$ aqueous solution in 70 °C for 30 min to post-treat. A dye was loaded on the film

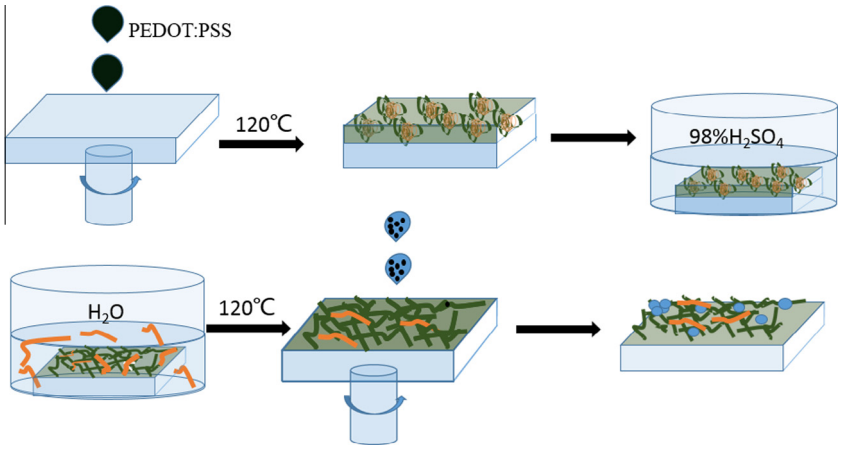

Fig. 1. The preparation process of counter electrodes.

by immersing the TiO_2 film in a 0.3 mM dye N719 (Deysol, Australian and Golden Innovation Business Co) ethanol solution for 18–24 h, finally a dye-sensitized photoanode was prepared. A DSSC was assembled by using the methods as described previously (Wu et al., 2008a,b, 2007).

2.4. Characterization and measurements

The surface morphologies of counter electrodes were observed by a field emission scanning electron microscopy (FESEM, S-8000, HITACHI). The field emission scanning electron microscopy (FESEM) photos were carried out on a JME-2100 transmission electron microscope operating at an accelerating voltage of 200 kV. Energy-dispersive spectroscopy data (EDS) were recorded with an Oxford Link ISIS energy-dispersive spectrometer fixed on the microscope. X-ray diffraction (XRD) measurements were performed with a Bruker D8 Advance X-ray diffractometer using Cu Ka radiation ($\lambda = 1.5418$ Å). For X-ray photoelectron spectroscopy (XPS) measurements, a Thermo ESCALAB 250XI (with monochromatized Al Kα radiation and an energy resolution of 0.5 eV) was used.

To assess the electrochemical catalytic activities of HPP, PC, PN, PC-PP, PN-PP and Pt CEs in the reduction of triiodide, the cyclic voltammograms (CVs) of samples were measured in a three-electrode electrochemical cell with an electrochemical workstation (CHI 660C, Shanghai Chenhua Co., Ltd., China) by using a prepared counter electrode as working electrode, a platinum wire electrode as counter electrode and a saturated Ag/AgCl electrode as reference electrode in an acetonitrile electrolyte containing 0.05 M I_2, 0.1 M LiI, 0.6 M tetrabutyl ammonium iodide and 0.5 M TBP. The range of voltage in CV measurements is −1.0 to 2.0 V, and the scan rate is 50 mV s^{-1}.

Electrochemical impedance spectroscopy (EIS) was measured by using two identical electrodes, the same electrolytes as CV measurement and a 50 μm thickness Surlyn film was used to separate the films and to seal the cells. An electrochemical workstation (Zennium/IM6, Zahner, Germany) was used and the range of frequency was turned from 1 Hz to 100 kHz. Electrode's electrochemical impedance parameters, namely R_S, R_{CT}, C_{dl} and Z_N are measured by using their symmetric cells under dark conditions, where R_S is the ohmic series resistance; R_{CT} is the charge transfer resistance at the electrode electrolyte; C_{dl} is the electrical double-layer capacitor and Z_w is Nernst diffusion impedance of the I^-/I_3^- redox couple in the electrolyte. Tafel polarization measurements were carried out by similar method as the EIS tests.

Photovoltaic parameters of the DSSCs were recorded with KEITHLEY Model 2450 quick star guide under illumination by Newsport 91150V solar simulator (AM 1.5, 100 mW cm^{-2}). Monochromatic incident photon-to-electron conversion efficiency (IPCE) curves were measured as a function of wavelength from 300 nm to 800 nm using the Newport IPCE system (Newport, USA).

3. Results and discussion

3.1. Morphology and structure

Field emission scanning electron microscopy (FESEM) and the high resolution transmission electron microscopy (HRTEM) were applied to analyze the structure of counter electrode materials. Fig. 2(a) and (b) shows the surface morphology of PEDOT:PSS film without H_2SO_4 treated and the H_2SO_4-treated PEDOT:PSS (HPP), respectively. It can be seen that PEDOT:PSS film is composed of nanoparticles and the film is compact and smooth. After H_2SO_4 treated, mesoporous structure appeared in the film and the HPP exist in short rod-like shape on the FTO substrate (Fig. 2(b)). Fig. 2(c) and (d) shows the SEM images of PC-PP and PN-PP films. The PC-HN and PN-HN are observed on the PEDOT:PSS network, respectively. Some PN-HNs assembled into larger particles but PC-HNs dispersed well.

Fig. 2(e) and (f) shows the HRTEM image of PC-HN. The hollow architecture is clearly observed by the contrast between the shells and hollow interiors, and most particles show sphere shape. The diameters of the nanospheres are estimated to be 20–30 nm. The thicknesses of the shells are about 2 nm. In Fig. 2(g) and (h), PN-HN also have a

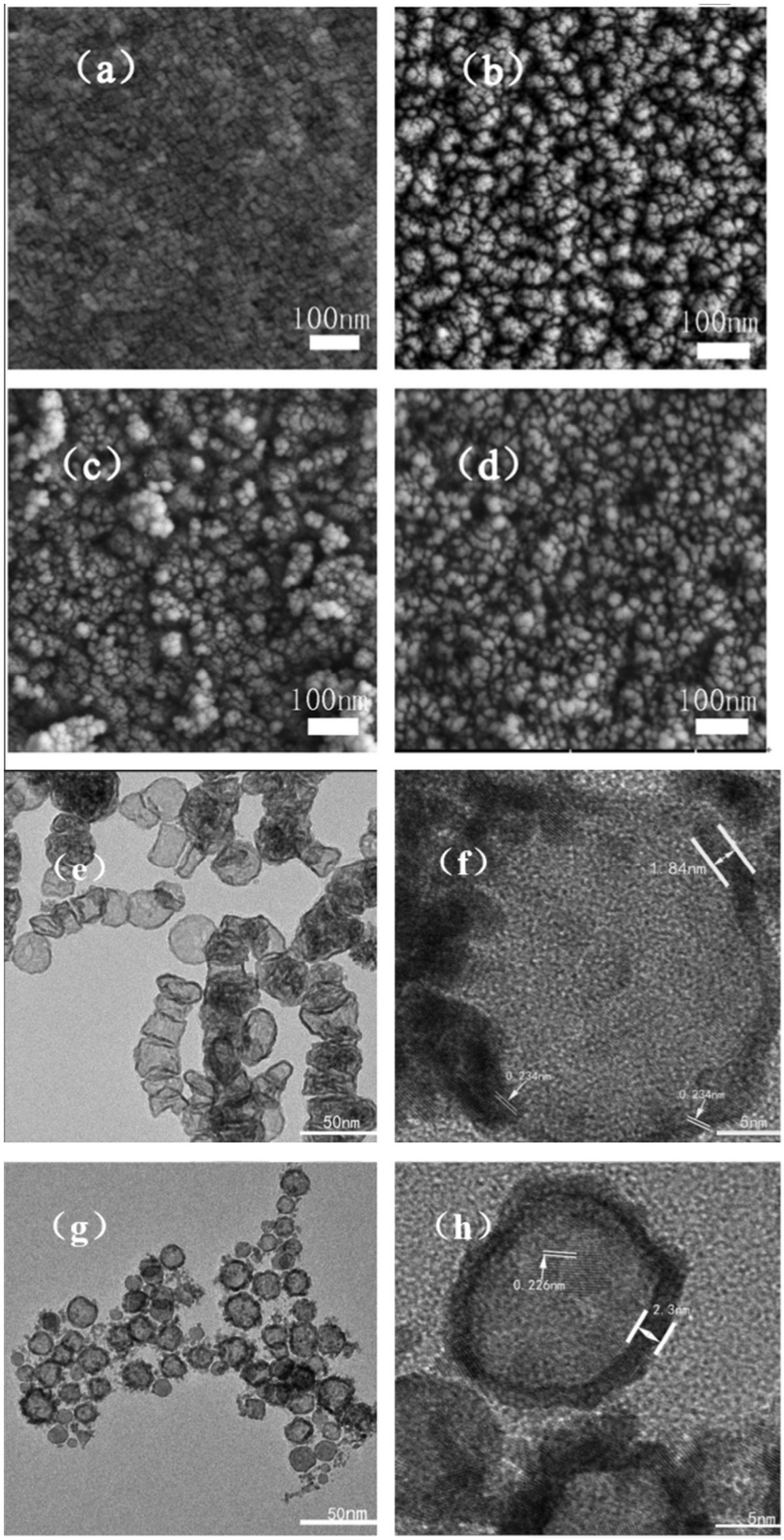

Fig. 2. SEM and HRTEM images of CE materials: (a) SEM of PEDOT:PSS without H_2SO_4-treated; (b) SEM of HPP; (c) SEM of PC-PP; (d) SEM of PN-PP; (e and f) HRTEM of PC-PP; and (g and h) HRTEM of PN-PP.

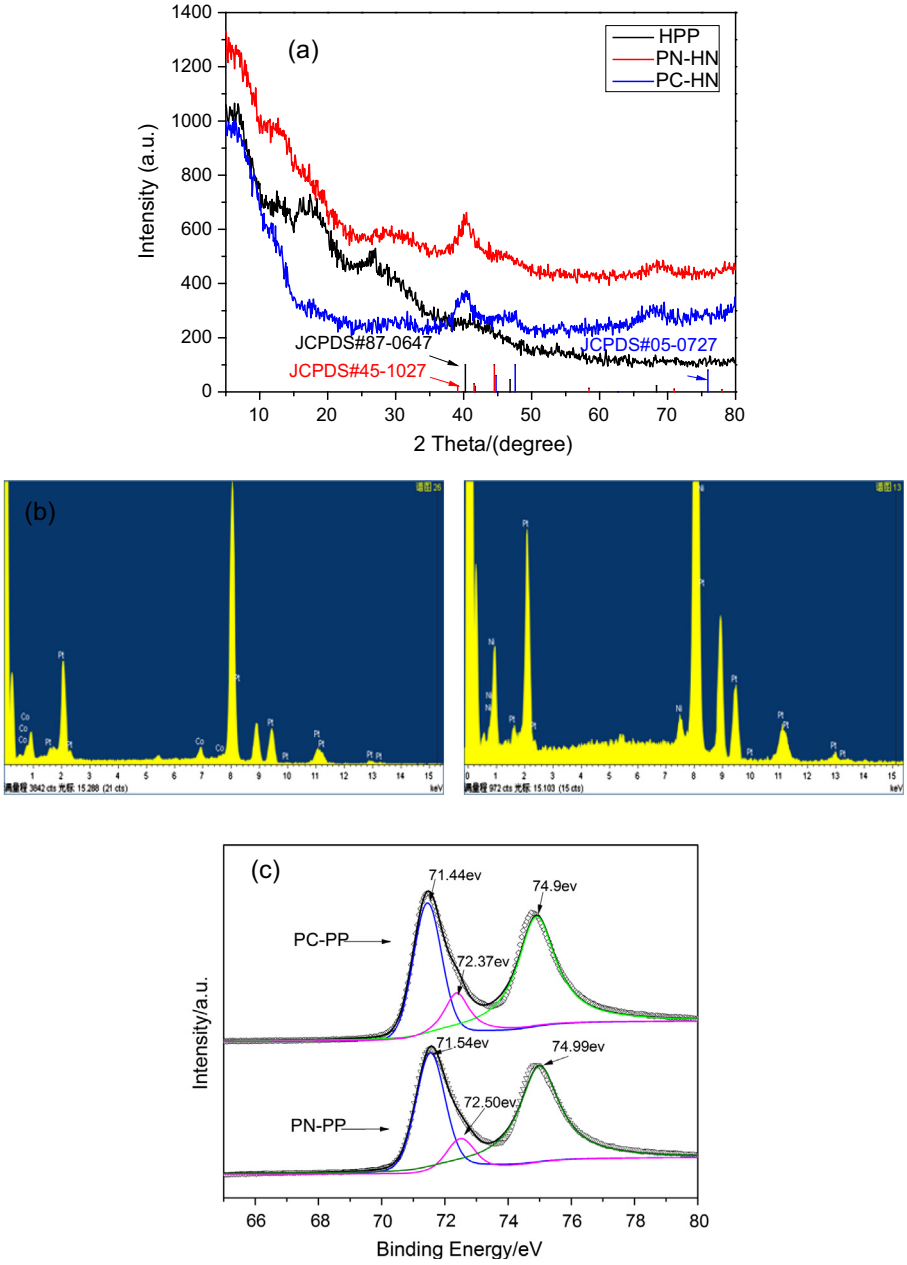

Fig. 3. (a) XRD of HPP, PN and PC; (b) EDS of PN and PC; and (c) XPS of PC-HN and PN-HN.

hollow structure, and most of them show sphere shape. However, several smaller particles are scattered around the hollow sphere. Comparing with the Pt–Co, the Pt–Ni hollow spheres have a smaller size, the diameter is about 12–18 nm. While, the thicknesses of the Pt–Ni spheres (about 2.3 nm) are larger than the Pt–Co spheres (about 1.8 nm). In addition, the Pt–Co and Pt–Ni have a dominant face centered cubic (fcc) crystal structure and the lattice fringe (1 1 1) about 0.230 nm from Fig. 2(f) and (h).

3.2. Phases and compositions

X-ray diffraction (XRD) spectroscopy was used to investigate the HPP, PN-HN and PC-HN. The broad peaks with low intensity in Fig. 3 indicate the poor crystallization of the sample. Fig. 3(a) shows the X-ray diffraction (XRD) pattern of H_2SO_4-treated PEDOT:PSS (HPP). Two characteristic diffraction peaks at about 17.7°, 25.6° are indexed to the amorphous halo of PSS and the interchain planar ring stacking distance $d_{(010)}$ of PEDOT, respectively (Kim et al., 2014). From the XRD patterns of the PN-HN and PC-HN, the peaks at about 39.8°, 46.2° and 67.4° are attributed to the Pt crystalline phase, which are consistent with the Pt phase planes (1 1 1), (2 0 0) and (2 2 0), respectively, according to (JCPDS card No. 87-0647). The low diffraction peak at 45.42° (in the red[1]

[1] For interpretation of color in Fig. 3, the reader is referred to the web version of this article.

spectroscopy) corresponds to the (0 1 1) planes of metallic Ni (JCPDS card No. 45-1027); the peaks at 47.56° and 75.9° (in the blue spectroscopy) attribute to the (1 0 1) and (1 1 0) planes of metallic Co (JCPDS card No. 05-0727).

To research the compositions of samples, energy-dispersive spectroscopy (EDS) was used. From Fig. 3(b), the atomic percentage ratio of Pt to Co is 20.6:79.4 in PC-HN, and the atomic percentage ratio of Pt to Ni is 17:83 in PN-HN, which indicate that the Pt has been incorporated with Co and Ni in the PC-HN and PN-HN film. The composition of Pt atoms in the as-prepared nanospheres was also analyzed by XPS. Fig. 3(c) shows the Pt $^4f_{7/2}$ and $^4f_{5/2}$ peak of hollow Pt binary alloy spheres. The Pt $^4f_{7/2}$ peak of PC-HN and PN-HN are at 71.44 and 71.54 eV, respectively. The peak at about 74.9 eV is attributed to Pt $^4f_{5/2}$. Moreover, the lower peak at 72.37 and 72.50 eV should be assigned to Pt $^4f_{7/2}$ of Pt atoms that are not completely reduced in PC-PP and PN-PP, respectively. Although there are few impurities, most of Pt atoms exist in alloy form due to their lager peak area.

3.3. Cyclic voltammograms (CVs)

Fig. 4(a) shows the CVs for six electrodes, in which two pairs of redox peaks can be observed for all of the six electrodes (the peak at about −0.5 V is due to the differential concentration near the electrode). The right pair represent the reaction of $I_3^- + 2e \leftrightarrow 3I^-$ on the counter electrode, which directly affects the DSSC performance (Bi et al., 2014), the absolute value of cathodic reduction peak current density ($|I_{RED1}|$) reflects the catalytic reaction velocity, and the peak-to-peak separation (E_{pp}) indicates with the potential of the catalytic reaction, associated with the overpotential of the catalytic reaction (Sun et al., 2010). The absolute value of cathodic reduction peak current density for different electrodes have following order: $|I_{RED1}|_{PC\text{-}PP}$ (0.902 mA cm^{-2}) > $|I_{RED1}|_{PN\text{-}PP}$ (0.853 mA cm^{-2}) > $|I_{RED1}|_{Pt}$ (0.847 mA cm^{-2}) > $|I_{RED1}|_{HPP}$ (0.683 mA cm^{-2}) > $|I_{RED1}|_{PC}$ (0.612 mA cm^{-2}) > $|I_{RED1}|_{PN}$ (0.489 mA cm^{-2}). Meanwhile, the E_{pp} values decrease in the order of PC-PP (0.469 V) < PN-PP (0.478 V) < PC (0.601 V) < HPP (0.612 V) < PN (0.64 V) < Pt (0.677 V). Comparing with HPP CE, both PC-PP CE and PN-PP CE have larger $|I_{RED1}|$ and smaller E_{pp}, suggesting that the PC-PP and PN-PP CEs have faster catalytic reaction velocity and good catalytic activity for the redox reaction, and introducing Pt–Co or Pt–Ni hollow nanospheres can improve the electrocatalytic activity of the PEDOT:PSS CE. Furthermore, the $|I_{RED1}|$ and E_{pp} values of Pt–Co and Pt–Ni supported by PEDOT:PSS are superior to Pt

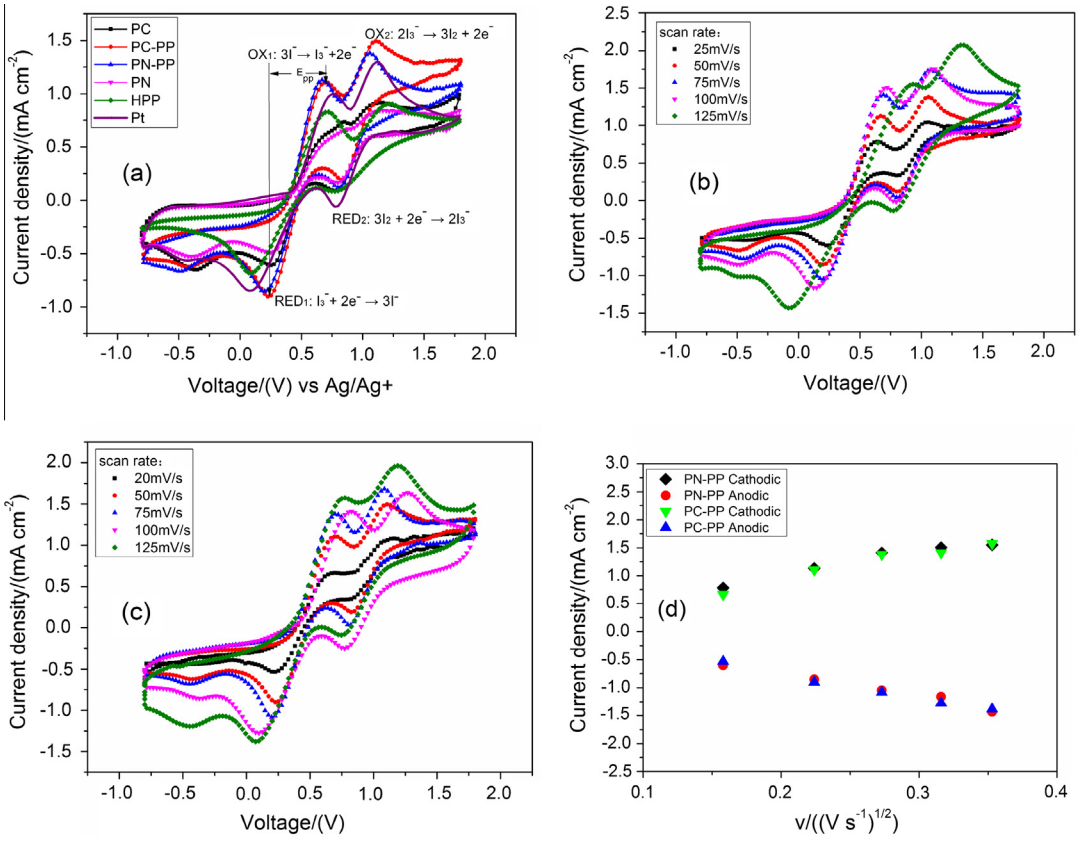

Fig. 4. (a) CVs for the PC-HN, PC-PP, PN-PP, PN-HN, HPP and Pt CEs at the scan rate of 50 mV s^{-1}, (b) CVs for the PN-PP with different scan rates (from inner to outer: 0.025, 0.050, 0.075, 0.100, and 0.125 V s^{-1}), (c) CVs for the PC-PP with different scan rates (from inner to outer: 0.025, 0.050, 0.075, 0.100, and 0.125 V s^{-1}), and (d) the redox peak current versus square root of scan rate.

CE. However, the electrodes of Pt–Co and Pt–Ni on FTO substrate show the smaller $|I_{RED1}|$ and larger E_{pp} values, which indicate that the support function of PEDOT:PSS.

Fig. 4(b) and (c) shows the CV curves for PN-PP and PC-PP electrodes at different scan rates. Based on the two CV curves form Fig. 4(b) and (c), Fig. 4(d) is obtained, the cathodic peaks current densities and anodic peaks current densities of PN-PP CE and PC-PP CE gradually and regularly shift to the negative and positive directions with increasing scan rate, respectively. Meanwhile, the current density versus (scan rate)$^{1/2}$ plots is almost linear, which suggests that the redox reactions on PN-PP and PC-PP CEs are a diffusion limitation reaction, and no specific interaction between I^-/I_3^- redox couple and the electrodes of Pt–Co or Pt–Ni on PEDOT:PSS (Sun et al., 2010).

3.4. Electrochemical impedance spectroscopy

Electrochemical impedance spectroscopy (EIS) measured results are shown in Fig. 5(a), the insert is an equivalent circuit diagram for fitting the Nyquist plots by the Zview software. The detailed EIS parameters are displayed in Table 1. Generally, the typical EIS plot of symmetric cells comprises of two semi-circles. The highest-frequency intercept on the real axis represents R_S and the first arc arises from R_{CT} and C_{dl}; Z_w can be observed from the second low-frequency semi-circle. As seen from Table 1, the R_S values for HPP, PC, PN, PC-PP, PN-PP and Pt CEs are 23.4, 12.5, 13.7, 12.6, 13.5 and 12.8 Ω cm^2, respectively. HPP CE has a larger R_S as a result of the relatively inferior conductivity compared with the Pt-based CEs. Introducing Pt–Ni hollow nanospheres or Pt–Co hollow nanospheres can improve the conductivity of HPP electrode. On the other hand, the R_{CT} values of the symmetric cells with HPP, PC, PN, PC-PP, PN-PP and Pt CEs are 4.23, 3.23, 4.51, 2.59, 2.97 and 2.63 Ω cm^2, respectively. This result suggest that the R_{CT} values of PN-PP and PC-PP CEs are closed to the value of Pt CE, which indicates PN-PP and PC-PP CEs have good catalytic performance as Pt CE. The C_{dl} value mainly depends on the surface area and the surface roughness of the CE. As expected, HPP coated with PN-HN and PC-HN can make the surface more rough and increase the surface area of the CE. As a result, PN-PP and PC-PP CEs have larger C_{dl} (0.525 and 0.377 mF cm^2, respectively) than HPP CE. On the other hand, owing to $Z_w < 2R_{CT}$ for PN and Pt electrodes, their semicircles in high frequency are larger than those in low frequency. The Z_w of PN-PP (5.52 Ω cm^2) and PC-PP (4.67 Ω cm^2) CEs are smaller than bare HPP (6.79 Ω cm^2), PN (8.27 Ω cm^2) and PC (15.6 Ω cm^2) CEs, but larger than Pt (1.58 Ω cm^2) CE. That is to say the diffusion coefficients (D) of triiodide for the cells vary in the inverse order, judged from Eq. (1), where k is the Boltzmann constant, T is the absolute temperature, n is the number of electrons involved in the electrochemical reduction of I_3^- at the electrode (here $n = 2$), e_0 is the elementary charge, c is the concentration of I_3^-, A is the electrode area, ω is the angular frequency, and δ is the thickness of the diffusion layer (Gong et al., 2012).

$$Z = \frac{kT}{n^2 e_0^2 cA\sqrt{i\omega D}} \tanh\left(\sqrt{\frac{i\omega}{D}}\delta\right) \quad (1)$$

Furthermore, we also utilize the Tafel polarization measurements to aid investigation the interfacial charge-transfer properties of the I^-/I_3^- redox couple on the CEs. In the Tafel curve (Fig. 5(b)), there are three zones: diffusion zone (horizontal zone in the curves), Tafel zone (in the middle potentials and with a sharp slope) and potential zone ($|U| < 0.120$ V). The exchange current density (J_0) which is estimated as the intercepting of the extrapolated linear region in Tafel zone when the over-potential is zero; the limiting current density (J_{lim}) can be obtained in the curve at high potential (horizontal zone) related to the catalytic activity of the catalysts. From Fig. 5(b) it can be seen that the slopes of the cathodic and anodic branches of the plots in the Tafel zone for the PC-PP, PN-PP and Pt electrodes are higher than PN, PC and HPP electrodes, exhibiting a larger J_0 for the former three electrodes than the latter three electrodes, suggesting that the former electrodes can catalysis the reduction of I_3^- to I^- more effectively than the latter electrodes. On the other hand, R_{CT} values of electrodes can

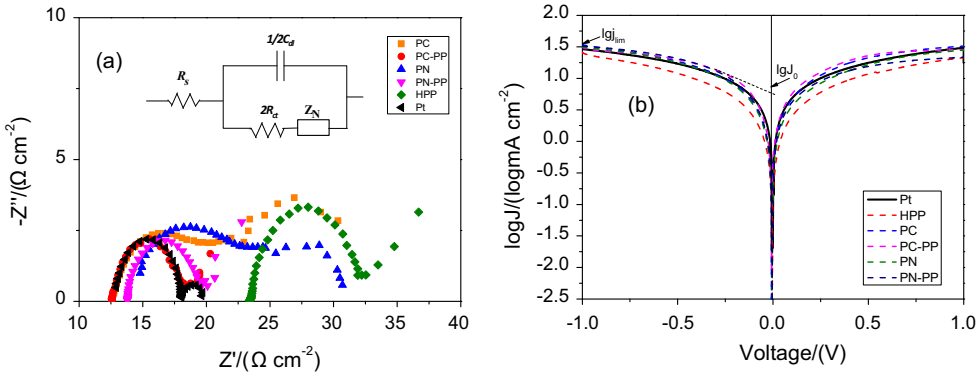

Fig. 5. (a) EIS measurements of the dummy cell fabricated with two identical Pt, PC, PC-PP, PN, PN-PP and HPP CEs and equivalent circuit model for I^-/I_3^- reaction and (b) Tafel curves of the symmetrical dummy cells fabricated with two identical electrodes.

Table 1
Electrochemical parameters for various counter electrodes.

Electrodes	Cell area (cm^2)	R_S ($\Omega\ cm^2$)	[a]R_{CT} ($\Omega\ cm^2$)	$1/2C_{dl}$ ($\mu F\ cm^2$)	Z_w (y_0) ($\Omega\ cm^2$)	[b]R_{CT} ($\Omega\ cm^2$)
HPP	0.32	23.4	4.23	0.318	6.79	4.06
PC	0.27	12.5	3.23	0.517	15.6	3.38
PN	0.20	13.7	4.51	0.421	8.27	3.62
PC-PP	0.21	12.6	2.59	0.377	4.67	2.03
PN-PP	0.23	13.5	2.97	0.525	5.52	2.28
Pt	0.40	12.8	2.63	0.0148	1.58	2.28

[a] The values obtained from EIS.
[b] The values obtained from Tafel plots.

be estimated from Tafel curve (Fig. 5(b)) according to Eq. (2), and the results are in accordance with the lower charge-transfer resistance R_{CT} measured by EIS.

$$J_0 = \frac{RT}{nFR_{CT}} \tag{2}$$

$$D = \frac{J_{lim}L}{2nFC} \tag{3}$$

The diffusion zone exhibit a similar J_{lim} except a slightly low one for the HPP CE. The relationship between the ionic diffusion coefficient D and J_{lim} can be expressed as in Eq. (3). Where R is the gas constant, T is the temperature, F is the Faraday constant, and n is the number of electrons involved in the reaction at the electrode, here, $n = 2$, C is the concentration of I_3^-, L is distance of electrodes. Based on Eq. (3), the diffusion coefficient (D) values for all electrodes can be obtained, and this proves that electrode holds a fast diffusion velocity of the redox couple in the electrolyte (Wang et al., 2014).

3.5. Photovoltaic performance of DSSCs

Fig. 6(a) shows the current density–voltage (J–V) curves of the DSSCs with different counter electrodes, and the resultant photovoltaic parameters are summarized in Table 2. The open circuit voltages (V_{OC}) of the DSSCs with different CEs do not show significantly different, and all V_{OC} values for the DSSCs with different CEs are about 0.74 V. The explanation is that the V_{OC} is mainly depended on the energy level between the Fermi level of the electron in the photoanode and the redox potential of the electrolyte (O'Regan and Gratzel, 1991). Because the anode films and electrolyte in all DSSCs have similar compositions, the V_{OC} values of all DSSCs are close. Notably, the cell with PC-PP CE shows a high short-circuit current density (J_{SC}) of 19.35 mA cm^{-2}, a fill factor (FF) of 0.626, and a power conversion efficiency (PCE) of 9.02%. The DSSC with PN-PP CE shows photovoltaic data of J_{SC}, FF and PCE are 18.04 mA cm^{-2}, 0.626% and 8.32%, respectively. The photovoltaic performance of the DSSCs based on the above two CEs are distinctly improved compared to the DSSC with Pt CE (PCE = 7.96%). Maybe, the high cathodic current density and the high active specific surface area could be responsible for the increase of J_{SC} and FF (Xiao et al., 2013; Saito et al., 2004). Comparing single HPP CE

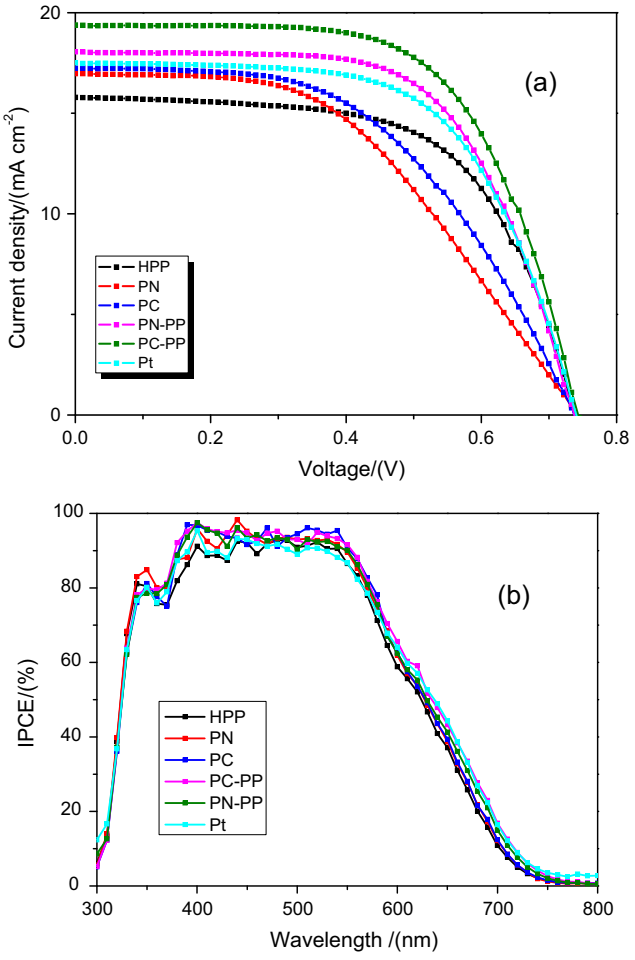

Fig. 6. (a) Photocurrent–voltage curves and (b) IPCE curves of the DSSCs based on different counter electrodes.

Table 2
Photovoltaic parameters of the DSSCs with different counter electrodes.

Electrodes	V_{OC} (V)	J_{SC} (mA cm^{-2})	FF	PCE (%)
HPP	0.742	15.79	0.61	7.15
PC	0.738	17.24	0.51	6.49
PN	0.740	17.00	0.47	5.91
PC-PP	0.744	19.35	0.63	9.07
PN-PP	0.736	18.04	0.63	8.36
Pt	0.742	17.49	0.61	7.92

and the CEs introduced hollow alloy nanospheres, not only a remarkable increase in J_{SC}, but also an slightly improved in FF, which results from the decreasing R_S and R_{CT} and the enhanced diffusivity of the I^-/I_3^- redox couple (He et al., 2014). While, the lower FF for the DSSCs based on PN and PC might due to their larger R_{CT} and discrete morphology. Therefore, Pt–Co and Pt–Ni binary alloy hollow nanospheres supported with PEDOT:PSS possess good photoelectron chemical feature and they can be developed to be promising counter electrodes for low-cost and highly efficient DSSCs.

In Fig. 6(b), we compare the IPCE curves of devices with different CEs in the wavelength range of 300–800 nm. The device with PC-PP CE exhibit a high broad peak (about 94%) from 380 to 560 nm followed by the DSSCs with PN-PP CE which show about 93% IPCE in the same range. In the wavelength range of 400–550 nm, the DSSCs based HPP, PC, PN and Pt CEs show about 90%, 94%, 93% and 91%, respectively. The IPCE results are accorded with the J_{SC} (Fig. 6(a) and Table 2).

3.6. Stability

To investigate the stabilities of PC-PP and PN-PP CEs, the consecutive 20 CV cycles are measured. Fig. 7(a) and (b) shows consecutive 20 CV cycle curves of the PC-PP and PN-PP CEs at scan rate of 50 mV s^{-1}. During the 20 successive CV cycles, no observable peak current change is found, suggesting that the PN-PP and PC-PP CEs are stably immobilized on the electrode. On 20 successive scans, though the peak current density changes with the scan voltage, the oxidation and reduction peak current scarcely show change, indicating that the CE is uniform and stably immobilized on the FTO glass and has an excellent electrochemical stability (the statistical results display in the insets).

To estimate the stability of the DSSCs based on PC-PP, PN-PP, the photovoltaic performances of the DSSCs based on PC-PP, PN-PP and Pt CEs were measured for continuous 10 h and the result is displayed in Fig. 7(c). It can be seen that the devices based on the three kinds of CEs have

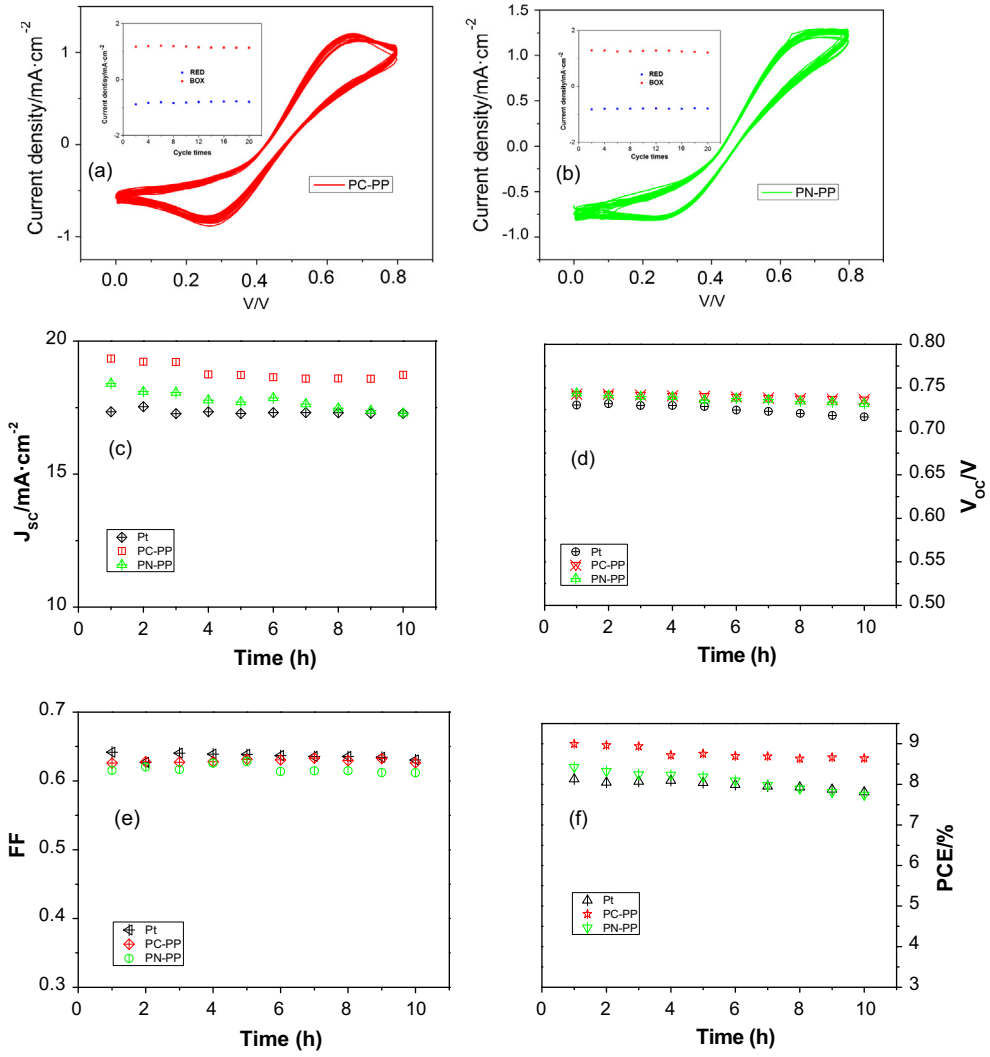

Fig. 7. CVs of (a) PC-PP and (b) PN-PP electrodes in scan rate of 50 mV s^{-1} for 20 time cycles (inserts: the relationship between the cycle times and the maximum oxidation and reduction peak currents); (c) J_{SC}, (d) V_{OC}, (e) FF, and (f) PCE versus test time for the DSSCs based on PC-PP, PN-PP and Pt CEs.

no large performance degradation. Compared with Pt CE, the J_{SC} of DSSCs with PC-PP and PN-PP both have slightly decreases and the PN-PP is more visible. However, the degradation of V_{OC} is clearly revealed for DSSCs based on Pt CE. FF values increase at first and then decrease for all of the three devices. As result, the PCE values of the DSSC based on PN-PP has the biggest declines due to the larger J_{SC} degradation and the DSSC with PC-PP CE has comparable stability to the DSSC with Pt CE.

4. Conclusion

In summary, we synthesis Pt–Co and Pt–Ni hollow nanospheres by using a simple solution method, and introduce these binary platinum alloys into the H_2SO_4-treated PEDOT:PSS as hybrid CEs (PC-PP and PN-PP) in the study. Two hybrid CEs possess both excellent electrocatalytic activity for the I_3^-/I^- redox reaction and high conductivity. The DSSCs based on PC-PP and PN-PP CEs show high power conversion efficiency up to 9.02% and 8.32%, respectively, which is increased by 13.3% and 4.5% compared to the DSSC based on Pt CE. The simple preparation method, few dosage of platinum and superior performance will provide a pathway for optimizing electrodes.

Acknowledgement

The authors gratefully acknowledge the financial supporting by the National Natural Science Foundation of China (Nos. 91422301, 51472094, 21301060, 61306077 and U1205112).

References

Ahmad, I. et al., 2014. Carbon nanomaterial based counter electrodes for dye sensitized solar cells. Sol. Energy 102, 152.
Anwar, H. et al., 2013. Vertically-aligned carbon nanotube counter electrodes for dye-sensitized solar cells. Sol. Energy 88, 129.
Bi, E. et al., 2014. A quasi core-shell nitrogen-doped graphene/cobalt sulfide conductive catalyst for highly efficient dye-sensitized solar cells. Energy Environ. Sci. 7, 2637.
Chen, D. et al., 2007. Facile synthesis of Co–Pt hollow sphere electrocatalyst. Chem. Mater. 19, 1840.
Chih, H. et al., 2012. Influences of textures in Pt counter electrode on characteristics of dye-sensitized solar cells. Org. Electron. 13, 199.
Chuang, H. et al., 2014. A coral-like film of Ni@NiS with core–shell particles for the counter electrode of an efficient dye-sensitized solar cell. J. Mater. Chem. A 2, 5816.
Cruz, R. et al., 2012. Reduced graphene oxide films as transparent counter-electrodes for dye-sensitized solar cells. Sol. Energy 86 (2), 716.
Gao, S. et al., 2014. Room temperature polymerization of poly (3,4-ethylenedioxythiophene) as transparent counter electrodes for dye-sensitized solar cells. Polym. Adv. Technol. 25, 1560–1564.
Gong, F. et al., 2012. In situ growth of Co(0.85)Se and Ni(0.85)Se on conductive substrates as high-performance counter electrodes for dye-sensitized solar cells. J. Am. Chem. Soc. 134, 10953.
Gong, F. et al., 2013. $NiSe_2$ as an efficient electrocatalyst for a Pt-free counter electrode of dye-sensitized solar cells. Chem. Commun. 49, 1437.
Gratzel, M., 2001. Photoelectrochemical cells. Nature 414, 338.
He, B. et al., 2014. Low-cost counter electrodes from Co Pt alloys for efficient dye-sensitized solar cells. ACS Appl. Mater. Interfaces 6, 4812.
Jiao, W. et al., 2014. Magnetic Ni and Ni/Pt hollow nanospheres and their catalytic activities for hydrolysis of ammonia borane. J. Mater. Chem. A 2, 18171.
Kim, N. et al., 2014. Highly conductive PEDOT:PSS nanofibrils induced by solution-processed crystallization. Adv. Mater. 26, 2268.
Li, P. et al., 2009. High-performance and low platinum loading Pt/carbon black counter electrode for dye-sensitized solar cells. Sol. Energy 83 (6), 845.
Li, Q. et al., 2008. Application of microporous polyaniline counter electrode for dye-sensitized solar cells. Electrochem. Commun. 10, 1299.
Liu, B. et al., 2009. Carbon nanotubes supported PtPd hollow nanospheres for formic acid electrooxidation. J. Power Sources 186, 62.
Lu, M. et al., 2014. Hierarchical nickel sulfide/carbon nanotube nanocomposite as a catalytic material toward triiodine reduction in dye-sensitized solar cells. J. Power Sources 270, 499.
O'Regan, B., Gratzel, M., 1991. A low-cost, high-efficiency solar cell based on dye-sensitized colloidal TiO_2 films. Nature 353, 737.
Pin, L. et al., 2008. High-performance and low platinum loading Pt/carbon black counter electrode for dye-sensitized solar cells. Sol. Energy 83, 845–849.
Que, L. et al., 2014. Titanium dioxide quantum dots: magic materials for high performance underlayers inserted into dye-sensitized solar cells. J. Power Sources 268, 670.
Saito, Y. et al., 2004. I^-/I_3^- redox reaction behavior on poly(3,4-ethylenedioxythiophene) counter electrode in dye-sensitized solar cells. J. Photochem. Photobiol. A 164, 153.
Sui, Y. et al., 2012. Nanoporous platinum counter electrodes by glancing angle deposition for dye-sensitized solar cells. Org. Electron. 13, 856–863.
Sun, H. et al., 2010. In situ preparation of a flexible polyaniline/carbon composite counter electrode and its application in dye-sensitized solar cells. J. Phys. Chem. C 114, 11673.
Wan, G. et al., 2014. Pt–Ni alloy nanoparticles as superior counter electrodes for dye-sensitized solar cells: experimental and theoretical understanding. Adv. Mater. 26, 8101.
Wang, L. et al., 2014. Composite catalyst of rosin carbon/Fe_3O_4: highly efficient counter electrode for dye-sensitized solar cells. Chem. Commun. 50, 1701.
Wu, J. et al., 2008a. High-performance polypyrrole nanoparticles counter electrode for dye-sensitized solar cells. J. Power Sources 181, 172.
Wu, J. et al., 2007. A novel thermosetting gel electrolyte for stable quasi-solid-state dye-sensitized solar cells. Adv. Mater. 19, 4006.
Wu, J. et al., 2008b. An all-solid-state dye-sensitized solar cell-based poly (N-alkyl-4-vinyl-pyridine iodide) electrolyte with efficiency of 5.64%. J. Am. Chem. Soc. 130, 11568.
Wu, J. et al., 2015. Electrolytes in dye-sensitized solar cells. Chem. Rev. 115, 2136.
Wu, M. et al., 2011. Low-cost molybdenum carbide and tungsten carbide counter electrodes for dye-sensitized solar cells. Angew. Chem. 50, 3520.
Xiao, Y. et al., 2013. Pulse electrodeposition of CoS on MWCNT/Ti as a high performance counter electrode for a Pt-free dye-sensitized solar cell. J. Mater. Chem. A 1, 1289.
Zi, Y. et al., 2012. High efficient PANI/Pt nanofiber counter electrode used in dye-sensitized solar cell. RSC Adv. 2, 4062.